Research Square

Preprints are preliminary reports that have not undergone peer review.
They should not be considered conclusive, used to inform clinical practice,
or referenced by the media as validated information.

Volcanic physics of nakhlite meteorites constrains density and thickness of the martian crust

Rongbin Yang
Peking University
Zilong Wang
Peking University
Wei Tian
davidtian@pku.edu.cn
Peking University
Lu Pan
University of Science and Technology of China
Yankun Di
The Australian National University
Bin Wang
Lanzhou University
Ao Su
Peking University
Ping-Ping Liu
Peking University
Wenzhe Fa
Peking University
Wei-(RZ) Wang
Chinese Academy of Geological Sciences
Chunjing Wei
Peking University

Article

Keywords:

Posted Date: November 9th, 2026

DOI: https://doi.org/10.21203/rs.3.rs-11344051/v1

License: This work is licensed under a Creative Commons Attribution 4.0 International License.
Read Full License

Additional Declarations: No competing interests reported.

Volcanic physics of nakhlite meteorites constrains density and thickness of the martian crust

Authors: Rongbin Yang[1], Zilong Wang[1,2], Wei Tian[1*], Lu Pan[3], Yankun Di[4], Bin Wang[5], Ao Su[1], Ping-Ping Liu[1], Wenzhe Fa[1], Wei-(RZ) Wang[2], Chunjing Wei[1]

Affiliations

[1] Research Institute of Extraterrestrial Materials, School of Earth and Space Sciences, Peking University, Beijing, China

[2] Key Laboratory of Paleomagnetism and Tectonic Reconstruction of MONR, Institute of Geomechanics, Chinese Academy of Geological Sciences, Beijing, China

[3] School of Earth and Space Sciences, University of Science and Technology of China, Hefei, China

[4] Research School of Earth Sciences, The Australian National University, Canberra, ACT 2601, Australia

[5] School of Earth Sciences, Lanzhou University, Lanzhou 730000, China

[*]Corresponding author: davidtian@pku.edu.cn

Abstract: The density and thickness of the Martian crust remain poorly constrained because gravity–topography inversions are inherently non-unique, only a single seismic anchor point is available at the InSight landing site, and no robust bound exists on the minimum permissible crustal density. Here we show that petrological observations, phase-equilibrium modeling and volcanic physics applied to two nakhlite meteorites, NWA 5790 and Qued Mya 005, constrain Martian crustal density and thickness through the buoyancy condition required for magma eruption. The minimum crustal density is 2852–2859 kg m^{-3}, corresponding to an average crustal thickness of 51.9–56.3 km and a minimum thickness of about 27 km at the eruption sites. Our results further identify Elysium Planum and North Tharsis Planum as source regions of young Amazonian volcanism and as priority targets for future landed missions, and they provide an independent perspective for constraining the crustal structure of terrestrial planets.

Introduction

The Martian crust is a critical archive for deciphering the planet's internal structure and a primary target of Mars exploration. Global mapping based on morphological and spectral data has documented widespread volcanic products across the surface[1]. The bulk crustal composition of Mars is broadly homogeneous, dominated by basaltic lithologies[2-4] with localized andesitic or felsic assemblages[5-7]. Prior to NASA's InSight mission, the bulk thickness and density of the Martian crust, together with their spatial variations, were constrained chiefly by two approaches: the gravity–topography admittance method[8-10], and a combined approach of spectral data and meteorite density constraints[11,12]. These studies yielded average crustal thickness estimates ranging from 30 km to more than 100 km and crustal densities spanning 2550–3100 kg m^{-3}. More recently, the Seismic Experiment for Interior Structure (SEIS) aboard the InSight lander has provided direct seismic constraints on Mars' interior[13,14]. Receiver function analyses reveal a three-layer crust beneath the InSight landing site with a total thickness of 39 km[15,16], and an updated reference model for the Martian mantle and core (the Khan 2022 model) has been developed from SEIS observations[17,18]. Anchored by these seismic constraints, the global average crustal thickness is estimated at 32–70 km, yet the estimate remains strongly dependent on the assumed uniform crustal density[19]. Most recently, seismic velocity analysis of the S1222a marsquake refined the average crustal thickness to 42–56 km and constrained large-scale crustal density variations to less than 200 kg m^{-3} [20].

Despite this progress, the seismic data currently available remain insufficient to resolve the bulk density of the Martian crust. A fundamental limitation of receiver function analyses as a density constraint is that crustal thickness models are inherently coupled to the assumed crustal density, and this degeneracy cannot be broken by a single seismic anchor point at the InSight landing site[19,21]. By requiring a positive crustal thickness beneath the major impact basins, the maximum permissible bulk crustal density has been bounded to 2850–3100 kg m^{-3} [16,19]. However, no robust constraint exists on the minimum bulk crustal density: published estimates range from as low as 2550 kg m^{-3} [22] to 3,100 kg m^{-3} [23]. This large uncertainty is primarily driven by variations in crustal porosity[2,12,21,24] and/or in the abundance of evolved felsic lithologies[2,5,16]. Importantly, the minimum permissible crustal density can, in principle, be constrained without deploying additional seismic stations on the Martian surface. From a volcanic physics perspective, magma can reach the surface only where the crust is sufficiently dense to permit buoyant ascent from a deep reservoir. Quantitative volcanic physics analyses of magma migration and eruption therefore offer an independent route to the minimum crustal density[25-27].

Such an approach, however, requires a magmatic system whose eruption is governed primarily by crustal processes. Nakhlites are a suite of Martian basalts that originate in the upper mantle, ascend buoyantly through the crust, and erupt onto the surface[28,29]. They are widely interpreted to share a common mantle source and magmatic evolution history, and consequently display consistent parental magma compositions and differentiation trends[29-31]. Recent Ar-Ar geochronology indicates that the nakhlites formed at ~1.34 Ga[28,32], and likely originated from young volcanic provinces on Mars, such as Tharsis or Elysium[1,10]. Geochemical constraints suggest nakhlites formed by low-degree partial melting of metasomatized lithospheric mantle, in contrast to shergottites, which are derived from deep mantle plumes[33,34]. This fundamental contrast implies that nakhlite eruption conditions are controlled more strongly by crustal properties than by mantle processes. In addition, recent petrological studies confirm that nakhlitic magmas were extruded onto the surface as lava flows, whereas chassignites were emplaced as shallow crustal

intrusions[28,35,36]. Together, these characteristics make the nakhlites the most suitable Martian basaltic meteorite suite for constraining crustal density and thickness through volcanic physics.

In this study, we develop a volcanic physics framework, grounded in nakhlites, to constrain the density range of the Martian crust. The framework integrates three components: the excess pressure in the deep magma reservoir, the overpressure in the shallow magma chamber (which depends on magma–crystal density, crustal density, and crustal thickness), and the critical overpressure required for magma migration. The physical properties and the ascending pressure–temperature (P–T) path of nakhlite parental magmas are constrained by thermobarometry, thermodynamic calculations, and detailed petrological and mineralogical investigations of two nakhlite samples: the rapidly cooled NWA 5790 and the newly identified, slowly cooled Qued Mya 005. We then evaluate global crustal density–thickness models to determine the minimum permissible bulk density of the Martian crust. Combined with density bounds from seismic constraints, the crustal density constraints derived here advance our understanding of Martian crustal properties and young basaltic volcanism.

Results and discussion

Petrology and nakhlite crystallization history

Petrological observations show that NWA 5790 and Qued Mya 005 record markedly different cooling histories and occupy discrete stratigraphic positions within the nakhlite lava pile, together providing complementary constraints on the crystallization sequence of nakhlitic magmas. NWA 5790 consists of euhedral to subhedral phenocrysts of clinopyroxene, olivine, and Fe–Ti spinel within a mesostasis of K-feldspar, silica, and Na-rich glass of plagioclase affinity (Fig. 1a,c). A diagnostic feature of this sample is its high modal abundance of glassy mesostasis, a trait shared with previously reported nakhlites such as NWA 817[37] and the Miller Range meteorites[38]. Combined with cooling-rate comparisons against other nakhlite specimens, this similarity places NWA 5790 in the upper portion of the nakhlite lava pile, where cooling was rapid and quenching prominent (Text S1,2). Qued Mya 005, by contrast, exhibits a more complex texture dominated by subhedral to anhedral phenocrysts of clinopyroxene, olivine, Fe–Ti spinel, and plagioclase (Fig. 1b,d), with distinctive features that include orthopyroxene coronas rimming olivine, K-rich glass filling intercrystalline voids as mesostasis, and clay minerals preferentially replacing olivine. Its modal glass content (2.3%) is nearly an order of magnitude lower than that of NWA 5790 (24.2%), and ilmenite lamellae exsolved from host Fe–Ti spinel are more extensively developed and thicker (Fig. 1c,d). Together, these textural and mineralogical features point to a protracted thermal annealing history, consistent with slowly cooled, deeply buried nakhlites such as NWA 998[29,39]. Coupled with the preservation of residual glass, this annealing signature further indicates an origin for Qued Mya 005 in the lower, most probably basal, portion of the nakhlite lava pile (Text S1,2). The two specimens thus form a complementary suite that spans the full vertical extent of the nakhlite lava flow sequence: the rapid cooling recorded by NWA 5790 preserves primary features of the early, high-temperature crystallization stages, whereas the prolonged cooling recorded by Qued Mya 005 archives late-stage subsolidus re-equilibration. Integrating textural and mineralogical data from both the rapidly and slowly cooled endmembers therefore allows the intrinsic crystallization sequence of nakhlitic magma to be reconstructed, independent of the textural artifacts imposed by variable cooling rates.

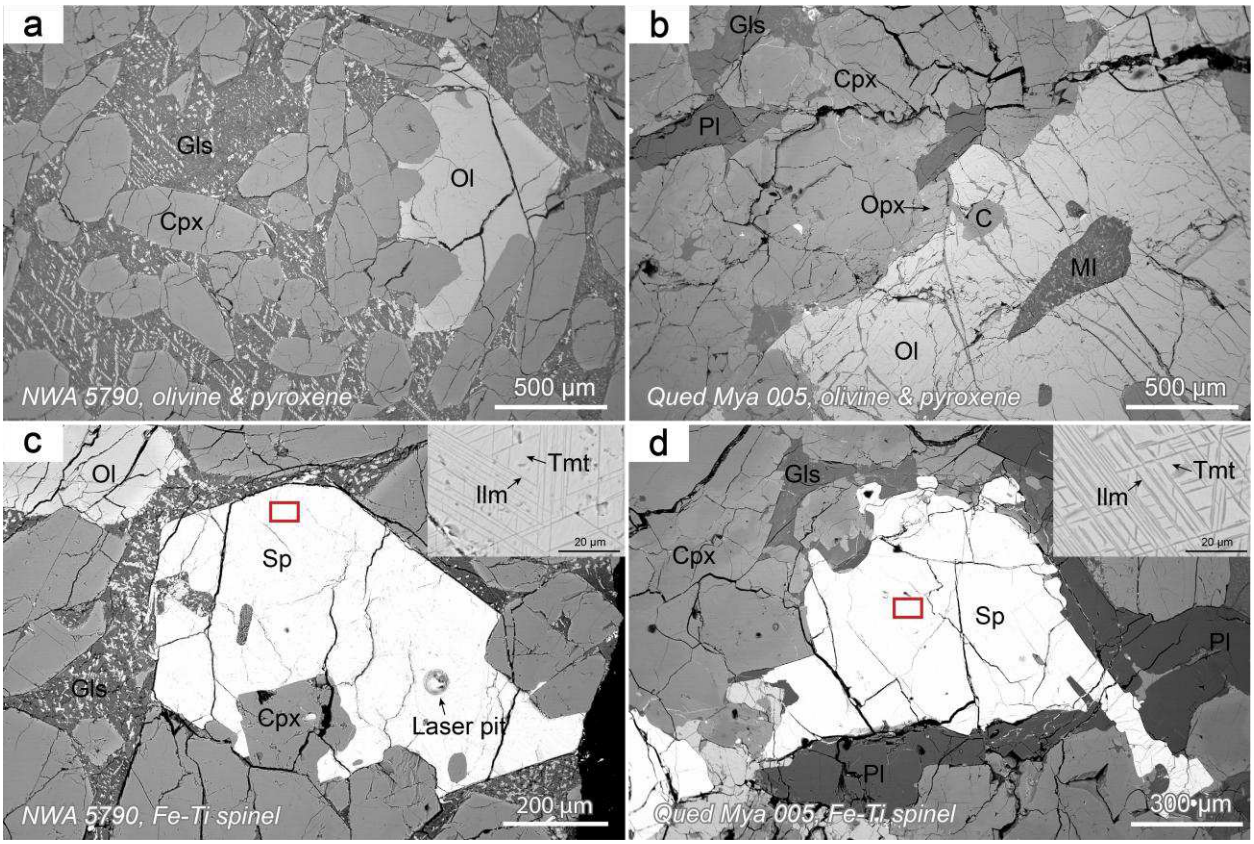


Fig. 1 | Backscattered electron images of the nakhlites NWA 5790 and Qued Mya 005. Panels **a** and **b** show the enclosure relationships among clinopyroxene, olivine, and glass. Panels **c** and **d** show the morphology of representative Fe–Ti spinel grains. The small insets in the upper right of panels **c** and **d** are magnified views of local areas of Fe–Ti spinel, the positions of which are indicated by red rectangles. Abbreviations: Ol, olivine; Cpx, clinopyroxene; Opx, orthopyroxene; Pl, plagioclase; Gls, glass; Sp, Fe–Ti spinel; Ilm, ilmenite; Tmt, titanomagnetite; MI, melt inclusion; C, clay; Laser pit, laser ablation pit.

The crystallization chronology of the nakhlite magma is further constrained by phenocryst–mesostasis relationships and diagnostic poikilitic textures (Text S4). During the earliest, high-temperature phenocryst stage, the partial enclosure of olivine by clinopyroxene cores and mutual textural contacts between the two phases indicate that clinopyroxene nucleated either synchronously with or slightly before olivine (Fig. 1a,b). Fe–Ti spinel, which typically encloses clinopyroxene partially, is more anhedral than olivine, and is commonly associated with mesostasis (Fig. 1c,d), thus crystallized immediately after olivine within this stage. During the subsequent residual-melt stage, the mesostasis of both samples is dominated by plagioclase and K-feldspar, both of which postdate the full phenocryst assemblage of clinopyroxene, olivine, and Fe–Ti spinel. In Qued Mya 005, plagioclase forms relatively coarse mesostasis crystals, whereas K-feldspar occurs as microcrystals or amorphous glass in both samples; this distinction indicates that plagioclase crystallized before K-feldspar as the residual melt evolved. During the final subsolidus stage, ilmenite lamellae form within Fe–Ti spinel by subsolidus exsolution[40] and thus represent the last textural modification in nakhlite formation. In summary, the crystallization sequence resolved for both Qued Mya 005 and NWA 5790 is clinopyroxene, olivine, Fe–Ti spinel, plagioclase, K-feldspar, and ilmenite. This order is consistent with that documented for other nakhlites, implying a common and potentially universal formation model for nakhlite

meteorites[28,29], and its persistence across samples with disparate cooling histories further supports a shared petrogenetic process.

Phase equilibria and ascent path of the nakhlitic magma

Phase equilibrium modeling was used to constrain the crystallization sequence and pressure – temperature (P–T) evolution of the nakhlite parental magma. After systematic validation (see Text S3), an optimized parental melt composition, PTL53, was selected for the modeling. This composition was derived from the bulk chemistry of olivine-hosted melt inclusions in the Nakhla meteorite and calibrated to be in equilibrium with primitive olivine (Fo_{53}) following established methods[41]. The modeling reveals a pressure-controlled crystallization sequence. At pressures above 6 kbar, clinopyroxene is the sole liquidus phase and crystallizes first (Fig. 2). Below 6 kbar, clinopyroxene, olivine, and Fe–Ti spinel co-crystallize between 1020 and 1150 °C. As the temperature falls to ~1020 °C, plagioclase begins to crystallize, by which point ~50 wt.% of the magma has solidified. With further cooling, K-feldspar joins the crystallizing assemblage at ~950 °C, followed by orthopyroxene at ~900 °C; both remain accessory phases in the mesostasis. The magma reaches its solidus at ~900 °C (Fig. 2). Below 800 °C, subsolidus exsolution within Fe–Ti spinel produces ilmenite lamellae, representing the final stage of textural modification.

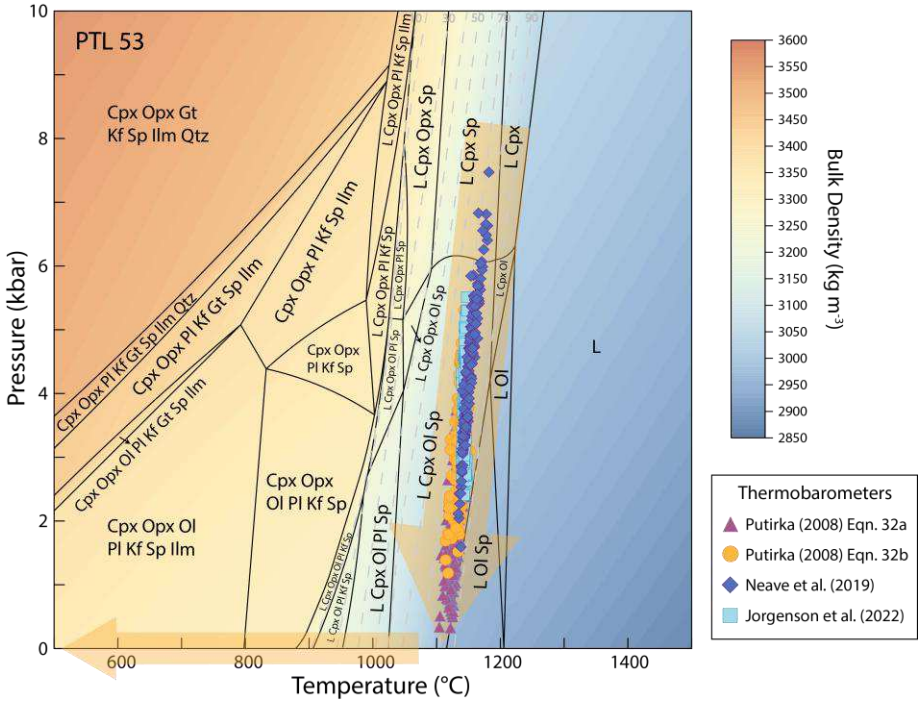


Fig. 2 | Isochemical pressure–temperature phase diagram (pseudosection) for the NCKFMASTOCr system (Na_2O–CaO–K_2O–FeO–MgO–Al_2O_3–SiO_2–TiO_2–Fe_2O_3–Cr_2O_3) system. The pseudosection was calculated for the starting composition PTL53 [41] and shows the stability fields of equilibrium assemblages. Dashed grey curves with numbers are isopleths of the melt mass fraction (wt.%). The colored background shows variations in bulk density across the pressure–temperature space. Results from single-clinopyroxene thermobarometers[42] and clinopyroxene–melt thermobarometers[43,44] are plotted as colored symbols, with shape and color distinguishing the individual models (legend). Translucent orange arrows indicate the magma ascent path. Abbreviations: L, liquid; Cpx, clinopyroxene; Opx, orthopyroxene; Ol, olivine; Pl, plagioclase; Kf, K-feldspar; Sp, spinel; Ilm, ilmenite; Qtz, quartz; Gt, garnet.

Independent thermobarometric estimates from single-clinopyroxene[42] and clinopyroxene–melt[43,44] calibrations consistently yield crystallization conditions of 1030–1170 °C and 0–6 kbar for most clinopyroxene cores, a range that is fully consistent with the clinopyroxene stability field defined by the phase equilibrium pseudosection (Fig. 2). Together with the modeling results, these P–T constraints define a well-resolved ascent path for the nakhlite parental magma from the Martian interior to the subsurface, fitted by the linear relation T (°C) = 7.79 · P (kbar) + 1114. Extrapolation of this path to the 0 kbar isobar yields an intersection temperature of 1114 °C, corresponding to magma eruption onto the Martian surface. Post-eruptive rapid cooling of the lava then drives crystallization of the mesostasis mineral assemblage (dashed orange arrows in Fig. 2). Along this ascent path, the bulk density of the magma – crystal mixture follows the linear relation ρ (kg m^{-3}) = 2.588 · T (°C) + 82.76. Ascent from 6 kbar (~60 km depth) to the surface (0 kbar) therefore causes a linear decrease in bulk density from 3100 kg m^{-3} to 2950 kg m^{-3}. After solidification, cooling below the solidus increases the density to more than 3300 kg m^{-3}, driven by complete crystallization and thermal contraction (Fig. 2).

Constraints on martian crustal thickness and density

The volcanic physics framework, detailed in the *Methods* section, provides quantitative constraints on the conditions required for magma eruption at the Martian surface. The core premise of the model is that nakhlitic magma can reach the surface only where the Martian crustal density is sufficiently high to maintain a positive residual magma pressure [Eqn. (4)]. The minimum permissible crustal density is therefore given by the intersection of the zero-isopleth of residual pressure with the crustal density–thickness relation at the nakhlite eruption site (Fig. 3a). This density–thickness relation is derived, for any given location, from geophysical inversions of gravity and seismic data integrated with reference models for mantle and core density[8,17]. The eruption site is located by linking the position of the ejection crater to the maximum travel distance of nakhlite lava flows. Crater counting combined with Ar–Ar geochronology places the nakhlite ejection crater at 130.799 °E, 29.674 °N, northwest of Elysium Planum[32], where the mean topographic slope is less than 1° [45]. Experimental petrology and magma rheology further indicate that a lava flow of nakhlite composition cannot travel more than 60 km across a 1° slope on the Martian surface[46]. At 30 °N on Mars, a 1° increment in both latitude and longitude corresponds to an area of about 50 km × 60 km, comparable to the maximum lava flow length. At a map resolution of 1° × 1°, the ejection and eruption sites are therefore geographically indistinguishable and may be treated as a single location.

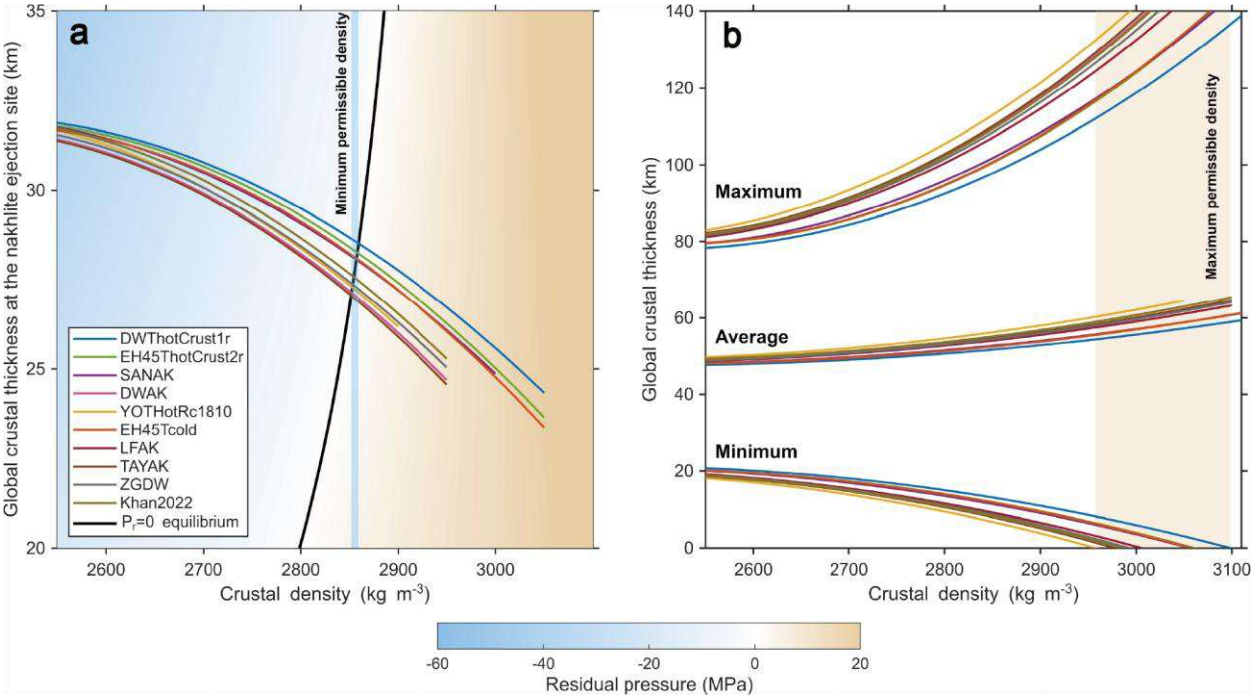


Fig. 3 | Estimated permissible range of Martian crustal density. **a**, Crustal thickness at the nakhlite ejection site (130.799 °E, 29.674 °N)[32] as a function of crustal density. The black curve is the zero-isopleth of residual pressure at the ejection site, and the colored curves are the crustal density–thickness relations at the ejection site for the different reference models. The intersections of the colored curves with the zero-pressure isopleth define the minimum permissible range of crustal density, shaded in blue. **b**, Global crustal density–thickness relations for the different reference models (colored curves). Maximum (upper), average (middle), and minimum (lower) crustal thickness are plotted as functions of the assumed crustal density, following the methodology of ref.[19]. As the global crustal density increases, the minimum crustal thickness decreases monotonically until it reaches zero. The maximum permissible crustal density is reached where the minimum crustal thickness effectively reduces to zero, and this range is shaded in orange.

Applying the inferred effusion site coordinates (130.799 °E, 29.674 °N) to the volcanic physics model yields a minimum permissible crustal density beneath the eruption site, with a mean value of 2855 kg m^{-3} (Fig. 3a and Table S3). Estimates vary slightly among the reference interior models, from 2852 kg m^{-3} (TAYAK model) to 2859 kg m^{-3} (DWThotCrust1r model) (Table S3). Assuming a uniform crustal density, this local constraint can be extended to the global scale. The global minimum density range (2852–2859 kg m^{-3}) corresponds to an average crustal thickness of 51.9–56.3 km. Regionally, maximum crustal thickness reaches 98.9–113.4 km at Daedalia Planum, and a minimum of 6.6–12.7 km at Hellas Planitia (Table S3). Analysis of crustal density–thickness trade-offs across reference interior models further shows that higher crustal densities amplify thespatial variations in crustal thickness, and systematically reduce the minimum crustal thickness beneath topographic lows (Fig. 3b). This monotonic relationship allows the maximum permissible crustal density to be quantified, as negative crustal thickness is physically implausible[19]. Across all reference models, the maximum permissible bulk crustal density is 3027 ± 71 kg m^{-3}, with individual model values ranging from 2957 kg m^{-3} (YOTHotRc1810 model) to 3098 kg m^{-3} (DWThotCrust1r model) (Fig. 3b and Table S4). The corresponding global average crustal thickness lies between 58.9 km and 60.3 km (Fig. 3b and Table S4).

A key caveat of extrapolating local density constraints to the global scale is the assumption of laterally uniform crustal density. This simplification is adopted because laterally heterogeneous models introduce substantial uncertainties and lack robust observational constraints[19]. The uniform density assumption is nevertheless geophysically plausible. First, volcanic provinces occupy a relatively small fraction of the Martian surface and are thus unlikely to significantly bias global average crustal density appreciably[19]. Second, recent seismic constraints indicate a density contrast of less than 200 kg m^{-3} between the northern lowlands and southern highlands[20], supporting the approximation of a globally constant crustal density for first-order constraints. Taken together, the constraints from volcanic physics and geophysical interior models define a permissible bulk crustal density range of 2855 ± 4 kg m^{-3} to 3027 ± 71 kg· m^{-3}, corresponding to a global average crustal thickness of 54.1 ± 2.2 km to 59.6 ± 0.7 km. These results are corroborated by recent seismic observations of the S1222a marsquake, which yield global average crustal thickness estimates of 42–56 km [20] or 43–63 km [47]. Further support comes from receiver function analyses: if the Martian crust is dominantly basaltic, its porosity is constrained to range from 7–10 vol.% [13] to 22–30 vol.% [24]. Assuming a pore-free crustal density of 3300 kg m^{-3} [19], the density bounds derived here imply a crustal porosity of 6–13 %, consistent with previous estimates. The crustal density constraints from the volcanic physics approach are therefore fully compatible with those from geophysical and seismic methods and provide a mutually consistent framework for understanding Martian crustal properties.

Implications for the compositions of amazonian lava flows

Nakhlites represent igneous products of the late Amazonian, the youngest geologic epoch on Mars[48]. Constraints on nakhlite eruption conditions provide quantitative insights into the spatial distribution of young Martian volcanic activity and its source regions. Calibrated by crystallization age, modeling across the full permissible range of crustal densities indicates that nakhlitic magma is capable of erupting within discrete segments of the northern lowlands, including Elysium Planum, North Tharsis Planum, and Amazonis Planitia (Fig. 4). This predicted distribution of eruption sites is consistent with independently proposed nakhlite ejection sites: 25 of the 52 documented sites lie in North Tharsis Planum and 22 in Elysium Planum. Both regions are dominated by lava flows rich in pyroxene, olivine, and glass[49], a mineral assemblage fully consistent with nakhlite petrology. Together, these spatial and petrological lines of evidence confine the source of young nakhlitic magmas to either Elysium Planum or North Tharsis Planum.

When crustal density is treated as a uniform parameter, a robust negative correlation emerges between residual magma pressure and crustal thickness, indicating that a thinner crust preferentially facilitates the eruption of nakhlitic magma (Fig. S10). Calculations based on the latest Khan 2022 reference model show that nakhlitic magma eruption is geophysically feasible only where the crustal thickness at the eruption site exceeds 27 km, given a minimum permissible crustal density of 2852 kg m^{-3} (Fig. S10). Recent seismic investigations have further identified localized partial-melt zones within the Martian interior that are spatially associated with crustal regions thicker than 60 km[20]. Such large crustal thicknesses would effectively prevent present-day nakhlitic magma from reaching the surface. Taken together, the critical crustal thickness threshold and the depth distribution of the partial-melt zones suggest that the probability of active nakhlitic magmatism at present is extremely low.

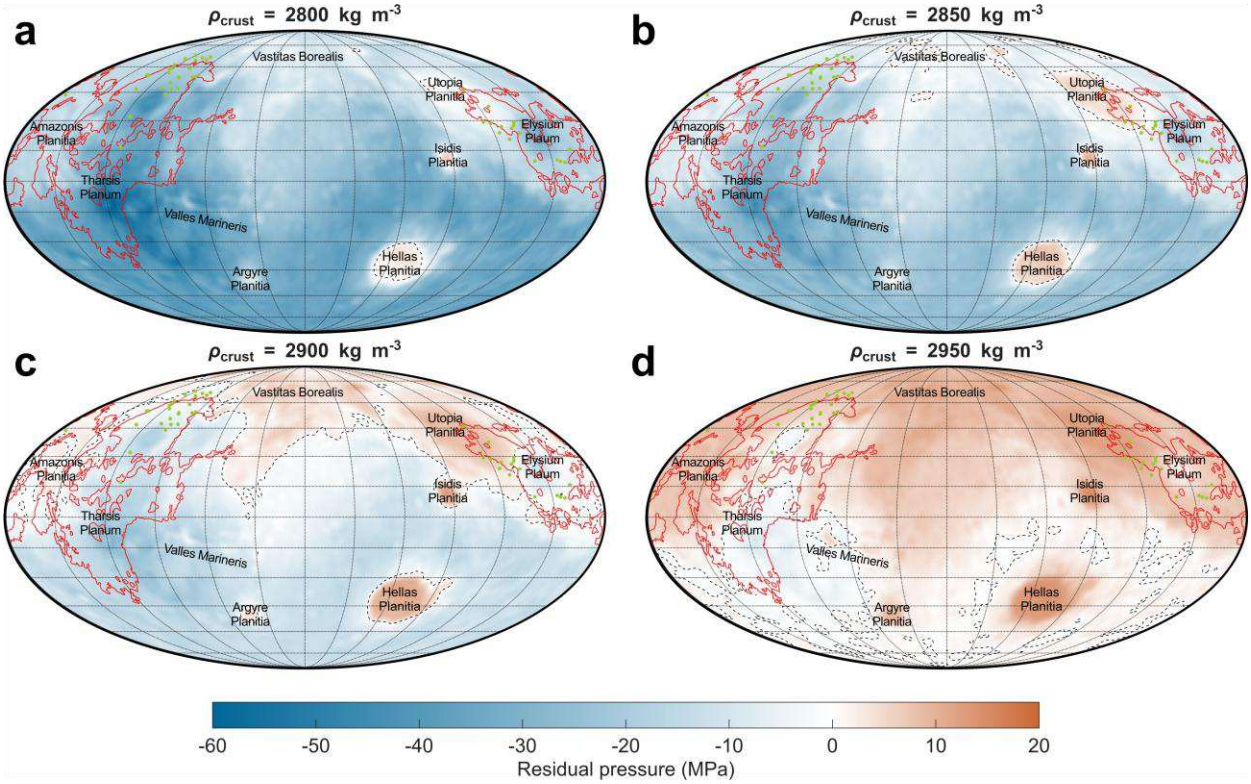


Fig. 4 | Global residual pressure distributions using the Khan2022 interior model[19].Panels **a**–**d** show the residual pressure distribution for crustal densities of 2800, 2850, 2900 and 2950 kg m^{-3}, respectively. The lowest value (**a**) is unrealistically low; **b** corresponds to the minimum permissible density (2852 kg m^{-3}) and **d** to the maximum permissible density (2957 kg m^{-3}), with the mapped densities rounded to the nearest 50 kg m^{-3}; **c** is an intermediate case. In each panel, black outlines mark the zero-isopleth of residual pressure, and red dashed outlines mark the Amazonian volcanic products on Mars[50]. The overlap between the two sets of outlines defines the potential eruption regions of nakhlitic magma. Green dots mark all possible nakhlite ejection sites identified from remote-sensing and geochemical measurements[32,45,51]. The maps are shown in Mollweide projection, with the color scale overlaid on a hillshade derived from surface topography[50] to provide geological context. Parallels and meridians are plotted at 15° and 30° intervals, respectively, with the central longitude and latitude at (0°, 0°).

Amazonian lava flows are widespread across Tharsis and Elysium Planum, where the crustal thickness commonly exceeds 100 km. This spatial pattern presents an apparent paradox with the thickness-dependent eruption constraint outlined above. One possible resolution is that the crustal density within these major volcanic provinces is substantially higher than the global average. Residual pressure calculations across a range of crustal densities show that, if the local crustal density exceeds 3000 kg m^{-3}, nakhlitic magma could erupt at any geologically plausible crustal thickness (0–140 km, Fig. S10). This hypothesis is corroborated by independent seismic and gravity data, which indicate that volcanic edifices can have bulk densities exceeding 3000 kg m^{-3} [52], and may even approach 3206 ± 190 kg m^{-3} [11].

Alternatively, the elevated apparent density of these provinces may reflect the high density of surficial lava flows, which typically have an aggregate thickness of only 20–60 m [53]. In this scenario, surficial lava flows contribute negligibly to the bulk crustal density, given their minimal thickness relative to the total crustal column. This implies that the extensive lava flows in these volcanic edifices must be compositionally distinct from nakhlites and derived from parental

magmas of significantly lower density that are able to ascend through thick crust. Basaltic shergottites, for example, are dominated by pyroxene and plagioclase and are widely interpreted to derive from surface lava flows[34]. Compared with nakhlites, shergottites are olivine-free, contain lower modal abundances of cumulus phases, and have SiO_2-rich, FeO-poor bulk compositions[54]. These geochemical characteristics correspond to lower parental magma densities than those of nakhlites, suggesting that the young lava flows in Tharsis and Elysium Planum are compositionally more similar to basaltic shergottites than to nakhlites. This interpretation is further supported by the numerical dominance of shergottites among Martian meteorites and by remote-sensing constraints that place shergottite ejection sites within central Tharsis Planum, adjacent to Olympus Mons or Ascraeus Mons[55].

Implications for the focal depth of volcanically induced marsquakes

Global models of Martian crustal thickness are conventionally constructed from orbital topography and gravity data in order to resolve spatial variations in crustal architecture, and are tied to seismic measurements at designated anchor points [24]. Yet the only such point presently available is the InSight landing site. Seismological constraints from this site have yielded estimates of local crustal thickness variations and of the thermal state of the Martian interior, but they all rest on an assumed uniform global crustal density of 2550–3200 kg m^{-3} [13,16,19,20,56,57]. Because crustal density is a governing parameter in these inversions, and existing seismic data cannot constrain it directly, the density must instead be assumed a priori. By adopting the nakhlite eruption site as a second, independent anchor point, this study defines the minimum permissible crustal density through volcanic physics simulations and thereby imposes robust bounds on the global crustal density range. Combined with the maximum permissible density constraints from geophysical and seismic methods[16,19], our results indicate that the average bulk crustal density of Mars most likely lies between 2900 and 3000 kg m^{-3}.

The crustal density constraints derived here also offer new insight into the bulk composition of the Martian crust. Andesitic rocks, whose typical density is ~2,800 kg m^{-3} [5], have been identified by in situ rover measurements and orbital imaging spectrometry[5,7,58], and widespread clay minerals detected by both orbital and in situ instruments may further lower the density of the near-surface crust[59]. Together, these observations have motivated the hypothesis that a low-density layer is buried beneath the denser basaltic surface layer[5,58], an interpretation supported by the average bulk crustal density of ~2582 ± 209 kg m^{-3} that Goossens et al. (2017)[22] inferred from topography–gravity correlations. Our results suggest otherwise: evolved, low-density components can account for only a minor fraction of the Martian crust, because most clay minerals and pore space are concentrated within the uppermost 10 km[21]. The deep crust should therefore be substantially denser than the 2900–3000 kg m^{-3} bulk average and consistent with the density of Martian basaltic rocks[12]. This inference reinforces the view that the Martian crust is predominantly basaltic, in line with early remote-sensing observations[3,4].

This study additionally offers guidance for future Mars rover exploration strategies. The constraints on crustal density and young volcanism presented above identify three promising targets for future investigation: Elysium Planum, North Tharsis Planum, and Amazonis Planitia, all candidate source regions of young Martian meteorites. To date, no landed mission has examined late Amazonian strata in this way. A lander equipped with a seismic instrument suite in one of these regions would establish a second geophysical anchor point, substantially improving the fidelity of global Martian crustal models by mitigating the degeneracy inherent in gravity and topography inversions[21]. Density estimates from receiver function analyses of marsquakes could

then independently validate the crustal densities inferred from volcanic physics, while surface exploration could reveal additional lithological analogues of Martian meteorites and resolve the detailed morphology of Martian lava flows. Such findings would advance our understanding of chemical variations among Martian igneous rocks and of the nature of young volcanism, thereby alleviating the sampling bias imposed by the limited source diversity of known Martian meteorites[28]. Comprehensive geochemical analysis of these regions would further constrain the formation and long-term evolution of the Martian crust and, in particular, illuminate the processes that produced its dominantly basaltic composition. The framework developed here thus provides an integrated, forward-looking perspective for the design of future Martian exploration missions.

Methods

Sample acquisition

Two sample slices, NWA 5790 (4.25 g) and Qued Mya 005 (15.7 g), were acquired in June 2020 from Luc Labenne and in March 2022 from Ziyao Wang, respectively. Both were selected from the fresh interiors of their parent masses and were free of discernible terrestrial carbonate and barite, ensuring the preservation of primary features with minimal terrestrial contamination. Each slice was prepared as a polished thin section and coated with a 20 nm-thick carbon film for subsequent analyses. The petrology and mineralogy of the two samples are described in Text S1 and S2 and illustrated in Figs. S1–S5.

TESCAN integrated mineral analysis (TIMA)

Mineral assemblages in the polished thin sections were identified with a TESCAN Integrated Mineral Analysis (TIMA) system at the Key Laboratory of Orogenic Belts and Crustal Evolution, School of Earth and Space Sciences, Peking University, China. The instrument comprises a TESCAN Mira Schottky field-emission automated scanning electron microscopy (ASEM) system with four silicon drift energy-dispersive (EDS) detectors arranged at approximately 90° intervals around the chamber. Analyses were performed in high-resolution liberation analysis mode using the following parameters: working voltage 25 kV, spot size 110 nm, working distance 15 mm, and field size 1000 μm. Backscattered electron (BSE) images were used to define individual particles and to distinguish boundaries between phases, and a rectangular mesh of X-ray spectral measurements was acquired for each phase.

Electron microprobe analysis (EPMA)

Quantitative chemical analyses of minerals in the polished thin sections were performed with a JEOL JXA-8230 electron microprobe at the Key Laboratory of Orogenic Belts and Crustal Evolution, School of Earth and Space Sciences, Peking University, using four wavelength-dispersive spectrometers. The accelerating voltage and beam current were 15 kV and 10 nA, respectively. The beam diameter was set to 1–5 μm, and a counting time of 20 s was used for both peak and background. The SPI 53 mineral standard (U.S.) was used for quantification, with the following calibrants: sanidine for K, diopside for Ca and Mg, rutile for Ti, jadeite for Na, Al, and Si, chromium oxide for Cr, rhodonite for Mn, hematite for Fe, and nickel silicide for Ni. Data were calibrated using a ZAF-based procedure. Detection limits of the oxides were 0.01 wt.% for K_2O, 0.02 wt.% for Al_2O_3 and Na_2O, 0.03 wt.% for MgO and CaO, 0.04 wt.% for TiO_2, Cr_2O_3, MnO, FeO, and NiO, and 0.06 wt.% for SiO_2. All EPMA data for the analyzed mineral phases are provided in Data S1.

Thermodynamic Modeling

All thermodynamic calculations were performed with GeoPS[60], a tool for self-consistent phase equilibrium calculations across the full composition space of a modeled system by Gibbs energy minimization. The modeling used the internally consistent end-member thermodynamic dataset of ds633[61] together with the activity–composition relationships of Holland2018[62], which allow both subsolidus and suprasolidus (melt-bearing) phase equilibria to be calculated for mafic igneous rocks such as the nakhlites. Calculations were performed in the system NCKFMASTOCr (Na_2O–CaO–K_2O–FeO–MgO–Al_2O_3–SiO_2–TiO_2–Fe_2O_3–Cr_2O_3), using recent thermodynamic models for olivine, pyroxene, feldspar, ilmenite, spinel, garnet, quartz, and melt. Although the Holland2018[62] models permit calculations in hydrous systems, an anhydrous subset was adopted, consistent with the water-poor nature of nakhlitic magma and the absence of hydrous minerals[34,63]. Oxygen fugacity was buffered at the Quartz-Fayalite-Magnetite (QFM) buffer, following the Fe–Ti oxide oxybarometer[64].

Twenty-three previously proposed parental magma compositions for nakhlites were then considered (Table S1) and modeled as starting compositions in GeoPS. The results were evaluated in terms of crystallization sequence, mineral equilibria, and the clinopyroxene pressure – temperature (P – T) path, which allowed the optimal parental magma composition to be identified. Phase equilibria and densities were subsequently computed with GeoPS for this composition over the modeled P – T space. Further details are given in Text S3.

Clinopyroxene thermobarometry

Clinopyroxene thermobarometry was used to delineate the ascent path of nakhlitic magma in pressure–temperature space. We compiled an EPMA dataset of major-element compositions (SiO_2, TiO_2, Al_2O_3, Cr_2O_3, FeO, MnO, NiO, MgO, CaO, Na_2O, K_2O) for nakhlite clinopyroxene (Data S2), comprising 714 analyses from 15 nakhlites, including the samples of this study and specimens reported previously[28,30,65,66] (Data S2). Two single-clinopyroxene models[42], one clinopyroxene–liquid model[43], and one machine-learning clinopyroxene–liquid model[44] were applied to this dataset using the open-source Python3 tool Thermobar[67]. For the basaltic system, the standard errors of estimate (SEE) of these models are below 2 kbar for pressure and below 50 °C for temperature. Before applying the clinopyroxene–liquid models, chemical equilibrium was evaluated for each clinopyroxene–liquid pair (Text S3), and P–T results from pairs that failed the equilibrium criteria were discarded. The pressure–temperature–density path of the nakhlite parental magma was then obtained by linear fitting of the valid thermobarometric P–T results using the MATLAB cftool, with magma density taken as a direct output of the GeoPS calculations.

Volcanic Physics Modeling

A parameterized model of dike propagation[68] was adopted to assess whether a given crustal density–thickness relation can support the eruption of nakhlitic magma. As illustrated in Fig. 5, nakhlitic magma is generated by partial melting of the mantle source and is temporarily stored in a deep magma reservoir, commonly at the crust–mantle interface, where it is retained by a buoyancy trap[33,34]. This configuration produces an excess pressure (P_e) that arises from the positive buoyancy of the magma in the upper mantle[27] and is described by

$$P_e = \int_D^{D+H} (\rho_M - \rho_m) g dz \quad (1)$$

where D represents the crustal thickness, H is the vertical extent of the melting region in the mantle, ρ_M and ρ_m are the densities of the mantle and magma, respectively, and g is the gravitational acceleration.

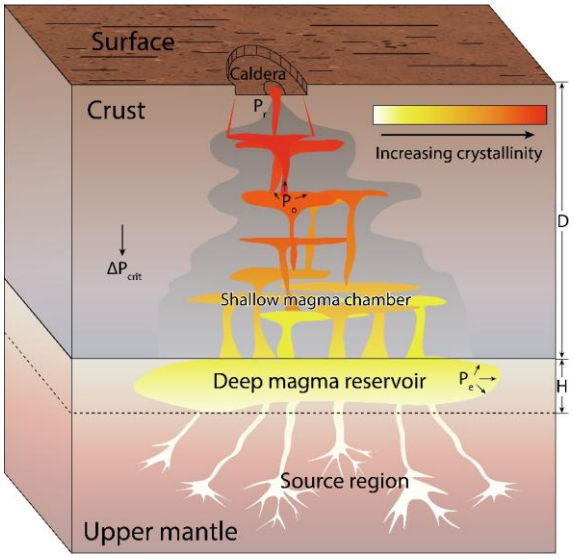


Fig. 5 | Schematic illustration of the volcanic physics model describing magma transport to the Martian surface. The diagram shows the crustal thickness (D) and the vertical extent of the melting region in the mantle (H). When magma reaches the surface, three key pressures are defined: the excess pressure in the deep magma reservoir (P_e), the overpressure in the shallow magma chamber (P_o), and the residual pressure at the surface ($P_o - \Delta P_{crit}$), where ΔP_{crit} is the critical overpressure. Colors indicate increasing crystallinity.

As the magma ascends within the crust and reaches the surface, the excess pressure may be altered due to crustal buoyancy and differential stress. The resulting overpressure (P_o) is given by[68] the following equation:

$$P_o = P_e + (\rho - \rho_m) g D + \sigma_d \quad (2)$$

where ρ is crustal density, σ_d is the differential stress.

The dike containing the magma can only reach the Martian surface if the overpressure within the propagating magma is sufficiently large. This condition ensures that the dike widens more quickly than it narrows due to freezing at its walls. The concept of critical overpressure (ΔP_{crit}) is introduced to encapsulate this idea. It represents the minimum pressure difference required to counteract the narrowing effect within the crust, thus enabling the magma to ascend to the surface[25]:

$$\Delta P_{crit} = 3.5 \left[\left(\frac{\kappa \mu_m}{\pi} \right)^{1/2} \frac{c |dT_{wr}/dx|}{L} E^2 \right]^{2/5} \quad (3)$$

where κ is the thermal diffusivity of the magma, μ_m is the magma viscosity, c is the heat capacity of the magma, dT_{wr}/dx represents the temperature gradient in the wall rocks along the dike path, L is the latent heat, and E is the Young's modulus of the wall rocks.

The concept of residual pressure (P_r) represents the pressure within the shallow magma chamber after overcoming the resistance of the surrounding crustal rocks. Specifically, it can be defined as the difference between the overpressure (P_0) and the critical overpressure (ΔP_{crit}).

Therefore, a necessary condition for the magma to reach the surface is that the residual pressure must be greater than zero:

$$P_r = P_0 - \Delta P_{crit} > 0 \quad (4)$$

The relationship between Martian crustal density (ρ) and thickness (D) was used to calculate the overpressure (P_0) and critical overpressure (ΔP_{crit}) and to evaluate the eruption condition in Eqn. (4). The parameters used in the volcanic physics modeling are detailed in Texts S4 and S5 and summarized in Table S2. Regionally resolved ρ–D relations for Mars were obtained from ten reference models of the Martian interior (DWThotCrust1r, EH45ThotCrust2r, EH45Tcold, SANAK, LFAK, ZG_DW, Khan2022, DWAK, TAYAK, and YOTHotRc1810)[8] combined with the parameterization of ref.[19], as described in Text S6. The modeling was performed with the MATLAB script "VolcPhyModel", and parameter uncertainties were propagated by Monte Carlo simulation using "SensTest", for which numerical stability improves as the number of iterations increases (Data S3). More than 10,000 randomized trials were run for each calculation to obtain robust uncertainty estimates, using the optimal parameters reported in Text S7. Global rasters of P_e, P_0, P_0–ΔP_{crit}, and ΔP_{crit} were then generated, excluding boundary conditions at 0°/360° longitude. Regions potentially supportive of nakhlite eruption were defined as those satisfying both Eqn. (4) and the crystallization-age constraint[32], and the resulting model was projected in the Mollweide projection with the MATLAB script "GlobResPres" (Data S3).

Refereces

1. Grott, M., et al. Long-Term Evolution of the Martian Crust-Mantle System. *Space Sci. Rev.* **174**, 49–111 (2012).
2. Thiriet, M., Michaut, C., Breuer, D. & Plesa, A. C. Hemispheric Dichotomy in Lithosphere Thickness on Mars Caused by Differences in Crustal Structure and Composition. *J. Geophys. Res. Planets* **123**, 823–848 (2018).
3. McSween, H. Y., Grove, T. L. & Wyatt, M. B. Constraints on the composition and petrogenesis of the Martian crust. *J. Geophys. Res. Planets* **108**, 5135 (2003).
4. McSween, H. Y., Taylor, G. J. & Wyatt, M. B. Elemental Composition of the Martian Crust. *Science* **324**, 736–739 (2009).
5. Sautter, V., et al. In situ evidence for continental crust on early Mars. *Nat. Geosci.* **8**, 605–609 (2015).
6. Morris, R. V., et al. Silicic volcanism on Mars evidenced by tridymite in high-SiO_2 sedimentary rock at Gale crater. *Proc. Natl. Acad. Sci. USA* **113**, 7071–7076 (2016).
7. Phillips, M. S., et al. Extensive and ancient feldspathic crust detected across north Hellas rim, Mars: Possible implications for primary crust formation. *Geology* **50**, 1182–1186 (2022).
8. Smrekar, S. E., et al. Pre-mission InSights on the Interior of Mars. *Space Sci. Rev.* **215**, 3 (2019).
9. Wieczorek, M. A. & Zuber, M. T. Thickness of the Martian crust: Improved constraints from geoid-to-topography ratios. *J. Geophys. Res. Planets* **109**, E01009 (2004).
10. Neumann, G. A., et al. Crustal structure of Mars from gravity and topography. *J. Geophys. Res. Planets* **109**, E08002 (2004).
11. Broquet, A. & Wieczorek, M. A. The Gravitational Signature of Martian Volcanoes. *J. Geophys. Res. Planets* **124**, 2054–2086 (2019).
12. Baratoux, D., et al. Petrological constraints on the density of the Martian crust. *J. Geophys. Res. Planets* **119**, 1707–1727 (2014).

13. Lognonné, P., et al. Mars Seismology. *Annu. Rev. Earth Planet. Sci.* **51**, 643–670 (2023).
14. Lognonne, P., et al. SEIS: Insight's Seismic Experiment for Internal Structure of Mars. *Space Sci. Rev.* **215**, 12 (2019).
15. Durán, C., et al. Seismology on Mars: An analysis of direct, reflected, and converted seismic body waves with implications for interior structure. *Phys. Earth Planet. Inter.* **325**, 106851 (2022).
16. Knapmeyer-Endrun, B., et al. Thickness and structure of the martian crust from InSight seismic data. *Science* **373**, 438–443 (2021).
17. Khan, A., et al. Upper mantle structure of Mars from InSight seismic data. *Science* **373**, 434–438 (2021).
18. Stähler, S. C., et al. Seismic detection of the martian core. *Science* **373**, 443–448 (2021).
19. Wieczorek, M. A., et al. InSight Constraints on the Global Character of the Martian Crust. *J. Geophys. Res. Planets* **127**, e2022JE007298 (2022).
20. Kim, D., et al. Global Crustal Thickness Revealed by Surface Waves Orbiting Mars. *Geophys. Res. Lett.* **50**, e2023GL103482 (2023).
21. Li, J., et al. Constraints on the martian crust away from the InSight landing site. *Nat. Commun.* **13**, 7950 (2022).
22. Goossens, S., et al. Evidence for a Low Bulk Crustal Density for Mars from Gravity and Topography. *Geophys. Res. Lett.* **44**, 7686–7694 (2017).
23. Semprich, J. & Filiberto, J. High-pressure metamorphic mineralogy of the Martian crust with implications for density and seismic profiles. *Meteorit. Planet. Sci.* **55**, 1600–1614 (2020).
24. Li, J., et al. Crustal Structure Constraints From the Detection of the SsPp Phase on Mars. *Earth Space Sci.* **10**, e2022EA002416 (2023).
25. Jellinek, A. M. & DePaolo, D. J. A model for the origin of large silicic magma chambers: precursors of caldera-forming eruptions. *Bull. Volcanol.* **65**, 363–381 (2003).
26. Wilson, L. & Head III, J. W. Mars: Review and analysis of volcanic eruption theory and relationships to observed landforms. *Rev. Geophys.* **32**, 221–263 (1994).
27. Wilson, L. & Head, J. W. Generation, ascent and eruption of magma on the Moon: New insights into source depths, magma supply, intrusions and effusive/explosive eruptions (Part 1: Theory). *Icarus* **283**, 146–175 (2017).
28. Udry, A. & Day, J. M. D. 1.34 billion-year-old magmatism on Mars evaluated from the co-genetic nakhlite and chassignite meteorites. *Geochim. Cosmochim. Acta* **238**, 292–315 (2018).
29. Treiman, A. H. The nakhlite meteorites: Augite-rich igneous rocks from Mars. *Geochemistry* **65**, 203–270 (2005).
30. McCubbin, F. M., et al. A petrogenetic model for the comagmatic origin of chassignites and nakhlites: Inferences from chlorine-rich minerals, petrology, and geochemistry. *Meteorit. Planet. Sci.* **48**, 819–853 (2013).
31. Corrigan, C. M., Velbel, M. A. & Vicenzi, E. P. Modal abundances of pyroxene, olivine, and mesostasis in nakhlites: Heterogeneity, variation, and implications for nakhlite emplacement. *Meteorit. Planet. Sci.* **50**, 1497–1511 (2015).
32. Cohen, B. E., et al. Taking the pulse of Mars via dating of a plume-fed volcano. *Nat. Commun.* **8**, 640 (2017).
33. Day, J. M. D., et al. Martian magmatism from plume metasomatized mantle. *Nat. Commun.* **9**, 4799 (2018).

34. Udry, A., et al. What Martian Meteorites Reveal About the Interior and Surface of Mars. *J. Geophys. Res. Planets* **125**, e2020JE006523 (2020).
35. Daly, L., et al. Understanding the emplacement of Martian volcanic rocks using petrofabrics of the nakhlite meteorites. *Earth Planet. Sci. Lett.* **520**, 220–230 (2019).
36. Griffin, S., et al. Constraints on the Emplacement of Martian Nakhlite Igneous Rocks and Their Source Volcano From Advanced Micro-Petrofabric Analysis. *J. Geophys. Res. Planets* **127**, e2021JE007080 (2022).
37. Sautter, V., et al. A new Martian meteorite from Morocco: the nakhlite North West Africa 817. *Earth Planet. Sci. Lett.* **195**, 223–238 (2002).
38. Hallis, L. J. & Taylor, G. J. Comparisons of the four Miller Range nakhlites, MIL 03346, 090030, 090032 and 090136: Textural and compositional observations of primary and secondary mineral assemblages. *Meteorit. Planet. Sci.* **46**, 1787–1803 (2011).
39. Treiman, A. H. & Irving, A. J. Petrology of Martian meteorite Northwest Africa 998. *Meteorit. Planet. Sci.* **43**, 829–854 (2008).
40. Wang, Z., Tian, W. & Di, Y. New temperature and oxygen fugacity data of Martian nakhlite from Northwest Africa (NWA) 5790 and implications for shallow sulphur degassing. *Earth Planets Space* **73**, 164 (2021).
41. Goodrich, C. A., Treiman, A. H., Filiberto, J., Gross, J. & Jercinovic, M. K_2O-rich trapped melt in olivine in the Nakhla meteorite: Implications for petrogenesis of nakhlites and evolution of the Martian mantle. *Meteorit. Planet. Sci.* **48**, 2371–2405 (2013).
42. Putirka, K. D. Thermometers and Barometers for Volcanic Systems. *Rev. Mineral. Geochem.* **69**, 61–120 (2008).
43. Neave, D. A., et al. Clinopyroxene–Liquid Equilibria and Geothermobarometry in Natural and Experimental Tholeiites: the 2014–2015 Holuhraun Eruption, Iceland. *J. Petrol.* **60**, 1653–1680 (2019).
44. Jorgenson, C., Higgins, O., Petrelli, M., Begue, F. & Caricchi, L. A Machine Learning-Based Approach to Clinopyroxene Thermobarometry: Model Optimization and Distribution for Use in Earth Sciences. *J. Geophys. Res. Solid Earth* **127**, e2021JB022904 (2022).
45. Mouginis-Mark, P. J., Zimbelman, J. R., Crown, D. A. & Garry, W. B. 4 - The Elysium Province. In: The Volcanoes of Mars). http://doi.org/10.1016/B978-0-12-822876-0.00008-4. Elsevier (2021).
46. Vetere, F., et al. Viscosity of Pyroxenite Melt and Its Evolution During Cooling. *J. Geophys. Res. Planets* **124**, 1451–1469 (2019).
47. Kim, D., et al. Structure Along the Martian Dichotomy Constrained by Rayleigh and Love Waves and Their Overtones. *Geophys. Res. Lett.* **50**, e2022GL101666 (2023).
48. Bibring, J.-P., et al. Global Mineralogical and Aqueous Mars History Derived from OMEGA/Mars Express Data. *Science* **312**, 400–404 (2006).
49. Viviano, C. E., et al. Composition of Amazonian volcanic materials in Tharsis and Elysium, Mars, from MRO/CRISM reflectance spectra. *Icarus* **328**, 274–286 (2019).
50. Tanaka, K. L., Robbins, S. J., Fortezzo, C. M., Skinner, J. A. & Hare, T. M. The digital global geologic map of Mars: Chronostratigraphic ages, topographic and crater morphologic characteristics, and updated resurfacing history. *Planet. Space Sci.* **95**, 11–24 (2014).
51. Kereszturi, A. & Chatzitheodoridis, E. Searching for the Source Crater of Nakhlite Meteorites. *Orig Life Evol Biosph* **46**, 455–471 (2016).
52. Kim, D., et al. Surface waves and crustal structure on Mars. *Science* **378**, 417–421 (2022).
53. Shoemaker Thackston, E. S., Carter, L. M., Garry, W. B., Morgan, G. A. & Plaut, J. J. New Insights Into Subsurface Stratigraphy Northwest of Ascraeus Mons, Mars, Using the

SHARAD and MARSIS Radar Sounders. *J. Geophys. Res. Planets* **127**, e2022JE007210 (2022).
54. McSween, H. Y., Head, J. W., Rogers, A. D. & Schmidt, M. E. Assessing global trends in Mars magma compositions using ground truth. *Meteorit. Planet. Sci.* **58**, 1306–1317 (2023).
55. Lagain, A., et al. The Tharsis mantle source of depleted shergottites revealed by 90 million impact craters. *Nat. Commun.* **12**, 6352 (2021).
56. Plesa, A. C., et al. Seismic Velocity Variations in a 3D Martian Mantle: Implications for the InSight Measurements. *J. Geophys. Res. Planets* **126**, e2020JE006755 (2021).
57. Egea-Gonzalez, I., et al. Regional heat flow and subsurface temperature patterns at Elysium Planitia and Oxia Planum areas, Mars. *Icarus* **353**, 113379 (2021).
58. Payré, V., Salvatore, M. R. & Edwards, C. S. An Evolved Early Crust Exposed on Mars Revealed Through Spectroscopy. *Geophys. Res. Lett.* **49**, e2022GL099639 (2022).
59. Ehlmann, B. L. & Edwards, C. S. Mineralogy of the Martian Surface. *Annu. Rev. Earth Planet. Sci.* **42**, 291–315 (2014).
60. Xiang, H. & Connolly, J. A. D. GeoPS: An interactive visual computing tool for thermodynamic modelling of phase equilibria. *J. Metamorph. Geol.* **40**, 243–255 (2021).
61. Holland, T. J. B. & Powell, R. An improved and extended internally consistent thermodynamic dataset for phases of petrological interest, involving a new equation of state for solids. *J. Metamorph. Geol.* **29**, 333–383 (2011).
62. Holland, T. J. B., Green, E. C. R. & Powell, R. Melting of Peridotites through to Granites: A Simple Thermodynamic Model in the System KNCFMASHTOCr. *J. Petrol.* **59**, 881–900 (2018).
63. Peslier, A. H., et al. Determination of the water content and D/H ratio of the martian mantle by unraveling degassing and crystallization effects in nakhlites. *Geochim. Cosmochim. Acta* **266**, 382–415 (2019).
64. Szymanski, A., Brenker, F. E., Palme, H. & El Goresy, A. High oxidation state during formation of Martian nakhlites. *Meteorit. Planet. Sci.* **45**, 21–31 (2010).
65. Krämer Ruggiu, L., et al. Caleta el Cobre 022 Martian meteorite: Increasing nakhlite diversity. *Meteorit. Planet. Sci.* **55**, 1539–1563 (2020).
66. Brian Balta, J., et al. Northwest Africa 5790: A previously unsampled portion of the upper part of the nakhlite pile. *Meteorit. Planet. Sci.* **52**, 36–59 (2017).
67. Wieser, P., et al. Thermobar: An Open-Source Python3 Tool for Thermobarometry and Hygrometry. *Volcanica* **5**, 349–384 (2022).
68. Gudmundsson, A. Volcanotectonics: understanding the structure, deformation, and dynamics of volcanoes. https://doi.org/10.1017/9781139176217. (Cambridge University Press, 2020).

Acknowledgments

Mingyue Gong and Xiaoli Li are thanked for assisting on EPMA analyses. Haiping Ren and Bo Zhang are thanked for assisting on TIMA analyses.

Funding

This work was supported by the National Natural Science Foundation of China grant 42272348 (WT)

Author contributions

W.T., R.B.Y. and Z.L.W. designed the study and developed the methodology; W.T. and Z.L.W. performed the investigation. R.B.Y., Z.L.W. and Y.K.D. prepared the visualizations. W.T., L.P.P., W.W. and C.J.W. supervised the research. R.B.Y. and Z.L.W. wrote the original draft. W.T., R.B.Y., Z.L.W., W.Z.F., Y.K.D. and L.P. reviewed and revised the manuscript. All authors discussed the results and commented on the manuscript.

Competing interests

Authors declare that they have no competing interests.

Data and materials availability

All data are available in the main text or the supplementary materials.

Additional information

This Supplementary information includes:

Supplementary Text

Figs. S1 to S10

Tables S1 to S4

References

Supplementary Data S1 to S3

Supplementary Files

This is a list of supplementary files associated with this preprint. Click to download.

- Supplementaryfile.docx
- SupplementaryData2.xlsx
- Volcphymodel.m